Kelli C. Kiekens
Wyant College of Optical Sciences,
University of Arizona,
Tucson, AZ 85721

David Vega
Wyant College of Optical Sciences,
University of Arizona,
Tucson, AZ 85721

Harrison T. Thurgood
Department of Aerospace and
Mechanical Engineering,
University of Arizona,
Tucson, AZ 85721

Dominique Galvez
Wyant College of Optical Sciences,
University of Arizona,
Tucson, AZ 85721

Davis J. McGregor
Department of Aerospace and
Mechanical Engineering,
University of Arizona,
Tucson, AZ 85721

Travis W. Sawyer
Wyant College of Optical Sciences,
University of Arizona,
Tucson, AZ 85721

Jennifer K. Barton[1]
Professor
Director BIO5 Institute,
Department of Biomedical Engineering,
University of Arizona,
Tucson, AZ 85721
e-mail: barton@email.arizona.edu

Effect of an Added Mass on the Vibration Characteristics for Raster Scanning of a Cantilevered Optical Fiber

Piezoelectric tube actuators with cantilevered optical fibers have enabled the miniaturization of scanning image acquisition techniques for endoscopic implementation. To achieve raster scanning for such a miniaturized system, the first resonant frequency should be of the order of 10 s of Hz. We explore adding a mass at an intermediate location along the length of the fiber to alter the resonant frequencies of the system. We provide a mathematical model to predict resonant frequencies for a cantilevered beam with an intermediate mass. The theoretical and measured data match well for various fiber lengths, mass sizes, and mass attachment locations along the fiber.
[DOI: 10.1115/1.4050691]

1 Introduction

Forward-looking, miniature endoscopic imaging systems have been enhanced by the recent introduction of scanning systems based on using quartered piezoelectric tube actuators (piezos) with cantilevered optical fibers. Such scanning systems take advantage of the inverse piezoelectric effect, which causes the piezoceramic material to exhibit a mechanical response, such as expansion and contraction, when a voltage is applied. Longitudinal quartering of the piezoelectrodes allows for four independent expansion/contraction surfaces. Applying an equal and opposite sinusoidal voltage across two opposing electrodes achieves a back-and-forth bending motion of the piezo. When a cantilevered fiber is held concentrically inside of a quartered piezo and the piezo is driven at the resonant frequency of the cantilevered fiber, the fiber tip deflection amplitude is enhanced. Mechanical amplification of several hundred times is possible when operating at the first resonant frequency. This amplification turns a few microns of deflection of the piezo into hundreds of microns of deflection or more at the fiber tip. Various scanning patterns, such as spiral, Lissajous, or raster, can be achieved through the control of the frequency and phase of the bi-axial electrodes present in a quartered piezo [1–3].

The major advantages of a piezoscanning system are the ability to electronically control the imaging field of view as well as the potential for higher resolution that can be achieved within the same diameter as miniature coherent fiber bundles or distal endoscopic tip charge-coupled devices (CCDs) [2]. The use of a variety of fiber types in the piezofiber system also provides the ability to utilize a variety of imaging modalities such as surface reflectance or fluorescence imaging, optical coherence tomography (OCT), and confocal or multiphoton microscopy (MPM).

Several researchers have already presented scanning fiber endoscope proof-of-concept designs for OCT, MPM, and wide field imaging [2,4–6]. Our lab is working to design and build a rigid endoscope capable of reflectance imaging, OCT, and MPM with a 1.5 mm diameter imaging channel utilizing a forward-looking scanning mechanism [7]. This endoscope could be useful in a variety of clinical applications, such as visualization of the ovaries and distal fallopian tubes where ex vivo studies suggest that ovarian cancer is detectable by fluorescence imaging, OCT, and MPM [8–12].

For a raster scan pattern, the two orthogonal axes of the quartered piezo are driven at different frequencies, a slow axis, and a fast axis. To acquire images at video rate, the slow axis should be of the order of 10 s of Hz (ideally 30–40 Hz) while the fast axis should be at least 100 times faster (in the kHz range). One method of achieving this is to have a system with a first resonant

[1]Corresponding author.

Contributed by the Applied Mechanics Division Technical Committee on Dynamics & Control of Structures & Systems (AMD-DCSS) of ASME for publication in the Journal of Engineering and Science in Medical Diagnostics and Therapy. Manuscript received October 5, 2020; final manuscript received February 8, 2021; published online April 22, 2021. Assoc. Editor: Mostafa Fatemi.

Copyright © 2021 by ASME

frequency in the 10's of Hz and a higher (e.g., third) resonant frequency in the kHz range. However, at the piezo and fiber dimensions required for a miniature endoscope, the first resonant frequency tends to be in the kHz range, rather than the 10 s of Hz as required.

End masses have been suggested by others to tailor vibrational parameters [13–15]. Other piezosystems include mass placements at the tip of the cantilevered fiber or a tube encasing some length of the fiber. These solutions work well when only the first resonant frequency is required, as is the case with a spiral or Lissajous pattern. However, these solutions are not suitable for higher order resonant frequencies. An end mass can create a nodal point around which the fiber tries to vibrate, thereby reducing the tip deflection [16], and a long single tube mass prevents the fiber from bending as required to produce higher order mode shapes.

In this paper, we examine the effects of an added mass at an intermediate location along the fiber on the resonant frequencies and tip deflection characteristics of a piezo-driven scanning fiber. We provide a mathematical model to predict the resonant frequencies of the system and compare the predicted values to measurements obtained from experimental setups. We show that an added mass on the fiber can provide another variable (besides piezo and fiber dimensions or material characteristics) to broaden the solution space for fiber scanning. These changes increase the suitability of a cantilevered fiber piezoscanning for use as part of a multimodality imaging endoscope system. The ability to predict the frequency allows us to tailor a mass geometry and location to produce the desired difference between the first and third resonant frequencies required for raster scanning. Ultimately, this approach can be used to design any scanning fiber system with an intermediate mass without the need for extensive experimental testing.

2 Methods

An optical fiber was modeled as a fixed-free beam, with a stainless-steel bead attached to the underside of the fiber at an intermediate location. To test the viability of using the first and third resonant frequencies to drive the scanning fiber in a raster pattern, we constructed a larger scale model of the proposed endoscopic fiber scanning system and placed a mass at the nodal point of the third resonant frequency. The motivation for this approach is that the mass can act as a forced nodal point, so by aligning it with a natural nodal point, that resonant frequency should be affected less than the other resonant frequencies, which do not share that nodal point in terms of the change in frequency and tip deflection. At the same time, a mass placement further from the base of the fiber will cause the first resonant frequency to decrease. The fiber can be driven both horizontally, as shown in the top image of Fig. 1, and vertically, as shown in the bottom image of Fig. 1.

2.1 Mathematical Derivation. Equations describing the motion of a beam with an intermediate and an end mass that have nonnegligible moments of inertia were derived by Hamdan et al. based on the Euler–Bernoulli beam theory [17]. In this approach, the beam is split into two segments, one from the base to the center of mass of the added mass (CoM), and the other from the CoM to the tip of the beam. This can be generalized to any number masses along the length of the beam by splitting it into additional segments and applying the correct boundary conditions. The interested reader may refer to the Appendix for more information. Both beam segments must individually satisfy the differential equation for simple harmonic motion

$$\frac{d^4 y_1}{dx_1^4} - \Lambda^4 y_1(x_1) = 0, \quad \text{for} \quad 0 \le x_1 \le l\eta \tag{1}$$

$$\frac{d^4 y_2}{dx_2^4} - \Lambda^4 y_2(x_2) = 0, \quad \text{for} \quad 0 \le x_2 \le l(1-\eta) \tag{2}$$

Here, y_1 describes the displacement of the beam in the driving direction from the base of beam to the CoM, and y_2 is the displacement of the beam in the driving direction from the CoM to the tip. η is the fractional distance along the beam from the base to the CoM and l is the length of the beam

$$\Lambda^4 = \frac{A\gamma\omega^2}{EI} \tag{3}$$

$$f = \frac{1}{2\pi}\Lambda^2\sqrt{\frac{EI}{A\gamma}} \tag{4}$$

where A is the cross-sectional area of the beam (πr^2), γ is the density of the material of the beam, ω is the resonant frequency of the beam in rad/s, E is Young's modulus of the beam material, I is the second moment of area of the beam, and f is the frequency in Hz. The general solution to the ordinary differential equations in Eqs. (1) and (2) is

$$\begin{aligned} y_1(x_1) = {} & \alpha_1 \sin(\Lambda x_1) \\ & + \alpha_3 \sin h(\Lambda x_1) + \alpha_4 \cos h(\Lambda x_1) \end{aligned} \tag{5}$$

$$\begin{aligned} y_2(x_2) = {} & \alpha_5 \sin(\Lambda x_2) \\ & + \alpha_7 \sinh(\Lambda x_2) + \alpha_8 \cosh(\Lambda x_2) \end{aligned} \tag{6}$$

Boundary conditions are imposed at the base of the beam ($x_1 = 0$), the CoM ($x_1 = l\eta$ and $x_2 = 0$), and at the end of the beam ($x_2 = l(1-\eta)$)

$$y_1(x_1 = 0) = 0 \tag{7}$$

$$\frac{dy_1(x_1 = 0)}{dx_1} = 0 \tag{8}$$

$$y_1(x_1 = l\eta) = y_2(x_2 = 0) \tag{9}$$

$$\frac{dy_1(x_1 = l\eta)}{dx_1} = \frac{dy_2(x_2 = 0)}{dx_2} \tag{10}$$

$$\begin{aligned} EI\frac{dy_1^2(x_1 = l\eta)}{dx_1^2} - EI\frac{dy_2^2(x_2 = 0)}{dx_2^2} \\ = J\omega^2\frac{dy_1(x_1 = l\eta)}{dx_1} \end{aligned} \tag{11}$$

$$\begin{aligned} EI\frac{dy_1^3(x_1 = l\eta)}{dx_1^3} - EI\frac{dy_2^3(x_2 = 0)}{dx_2^3} \\ = -\omega^2 M y_1(x_1 = l\eta) \end{aligned} \tag{12}$$

$$EI\frac{dy_2^2(x_2 = l(1-\eta))}{dx_2^2} = 0 \tag{13}$$

$$EI\frac{dy_2^3(x_2 = l(1-\eta))}{dx_2^3} = 0 \tag{14}$$

Here, J and M are the moment of inertia and mass of the added mass, respectively. J is used to evaluate a boundary condition at the location of the CoM, so additional moment of inertia from the offset distance from the base of the beam is not included. However, if using an asymmetric mass with respect to the overall system, as was used in this paper, the additional moment of inertia due to the offset of the CoM compared to the beam does need to be included using the parallel axis theorem for the direction for which the CoM does not align with the rotation axis. In the experimental setup described here, the horizontal axis is not affected by the offset, but the vertical axis is

$$J_{\text{Horizontal}} = J_{\text{mass}} \tag{15}$$

$$J_{\text{Vertical}} = J_{\text{mass}} + M\left(r_{\text{fiber}}^2 + r_{\text{mass}}^2\right) \tag{16}$$

Plugging in Eqs. (5) and (6) into Eqs. (7)–(14) produces a system of linear equations for the variables α_1 through α_8 which can be put into matrix form

$$\begin{bmatrix} 0 & 1 & 0 & 1 & 0 & 0 & 0 & 0 \\ 1 & 0 & 1 & 0 & 0 & 0 & 0 & 0 \\ \sin(Z_1) & \cos(Z_1) & \sinh(Z_1) & \cosh(Z_1) & 0 & -1 & 0 & -1 \\ \cos(Z_1) & -\sin(Z_1) & \cosh(Z_1) & \sinh(Z_1) & -1 & 0 & -1 & 0 \\ -A\gamma\sin(Z_1) & -A\gamma\cos(Z_1) & A\gamma\sinh(Z_1) & A\gamma\cosh(Z_1) & 0 & A\gamma & 0 & -A\gamma \\ -J\Lambda^3\cos(Z_1) & +J\Lambda^3\sin(Z_1) & -J\Lambda^3\cosh(Z_1) & -J\Lambda^3\sinh(Z_1) & & & & \\ -A\gamma\cos(Z_1) & A\gamma\sin(Z_1) & A\gamma\cosh(Z_1) & A\gamma\sinh(Z_1) & A\gamma & 0 & -A\gamma & 0 \\ +M\Lambda\sin(Z_1) & +M\Lambda\cos(Z_1) & +M\Lambda\sinh(Z_1) & +M\Lambda\cosh(Z_1) & & & & \\ 0 & 0 & 0 & 0 & -\sin(Z_2) & -\cos(Z_2) & \sinh(Z_2) & \cosh(Z_2) \\ 0 & 0 & 0 & 0 & -\cos(Z_2) & \sin(Z_2) & \cosh(Z_2) & \sinh(Z_2) \end{bmatrix}$$

Here, $Z_1 = \Lambda l\eta$ and $Z_2 = \Lambda l(1-\eta)$. The determinant of this matrix is then set equal to zero, and solutions for Λ are found. There are infinitely many solutions with the smaller values, greater than zero, referring to the lower order modes of the system. The values of Λ are then plugged into Eq. (4) to calculate the corresponding frequencies.

Since the damping ratio cannot be known without an experimental setup, the mathematical model assumes an undamped case. This analysis does not take into consideration the boundary conditions imposed by the base excitation from the piezo. Base excitation amplitude relates to the overall amplitude of the movement of the system, but is assumed to not significantly alter the resonant frequencies of the system [18,19].

2.2 Experimental Setup. The experimental setup consisted of a piezo (Boston Piezo, MA) with DCF13 fiber (Thorlabs, NJ) held in the piezo with a two-part epoxy (Fiber Instrument Sales, NY). The piezo was made from PZT-4 and was mounted in a custom three-dimensional printed part. A TD250 channel amplifier (Piezo-Drive, Callaghan, NSW, Australia), in conjunction with a waveform generator (Agilent, CA), was used to drive the piezo-fiber systems. The fiber length from the end of the piezo to the fiber tip was measured by taking an image of the system with a ruler just behind the fiber. In IMAGEJ (National Institutes of Health, USA), the mm markings on the ruler were used to set the scale of the image, then a line was drawn from the base of the fiber to the tip and was measured according to the scale. This procedure was repeated with multiple pictures to get an average length and a standard deviation, which was used as the measurement uncertainty. The length measurement and associated uncertainty were used as inputs for the mathematical model to obtain predicted ranges of resonant frequencies. The predicted frequency ranges provided a starting point for finding the resonant frequencies experimentally. Beginning near each predicted resonant frequency, the waveform generator was tuned coarsely by 1 Hz to find the approximate frequency, then fine-tuned by 0.1 Hz to find the frequency that produced the greatest deflection. There is an assumed $\pm 0.1\%$ uncertainty for the frequency measurements. Once the frequency was determined, the input voltage was turned off then stepped up from 0 to the maximum of RMS voltage of 179.2 V in 20 V increments.

Digital cameras (Nikon, Tokyo, Japan) were placed above and to the side of the fiber to capture the shape as it was excited at each resonant frequency to confirm the order that was excited

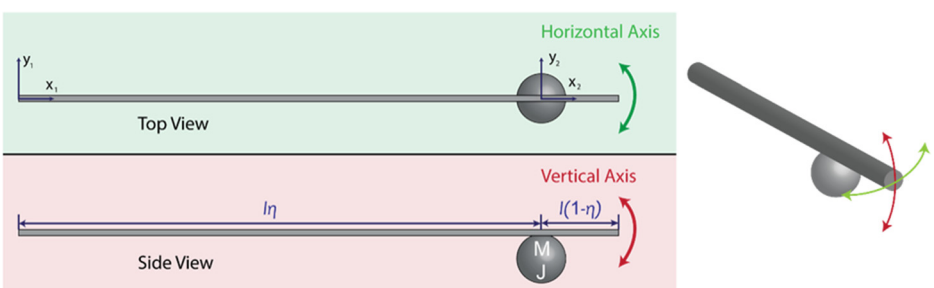

Fig. 1 A top (top) and side (bottom) view of the system investigated in this paper with the variables of the system labeled. To the right is a three-dimensional view of the system showing the axes being excited. The fiber is split into two segments, each with a new coordinate system (*x*1, *y*1) from the base of the fiber to the CoM, and (*x*2,*y*2) from the CoM to the tip of the fiber. *l*—beam length, *lη*—length from the base of the fiber to the CoM, *l*(1−*η*)—length from the CoM to the fiber tip, M—mass of the added mass, J—moment of inertia of the added mass, and CoM—Center of mass.

(i.e., first, second, third,…), and a high-speed camera (FastCAM Mini AX 200, Tokyo, Japan) was focused on the fiber tip. This setup is shown in Fig. 2. An image of a still fiber was used to calibrate the images within the FASTCAM software by converting number of pixels to microns using 105 μm outer diameter of the first clad of the DCF13 fiber as the known reference. A still image obtained by setting an exposure time that could show the full path of the fiber tip was acquired. Then using the measuring tool within the software, a line was drawn between the extreme edges and the length of the line, which is equal to the total deflection, was obtained directly from the software.

Once the experimental results were acquired with the massless fiber system, a stainless-steel bead (Cospheric, CA) was weighed, then glued at the approximate location of the node of the third resonant frequency. The location of the mass was determined in the same way as the length of the fiber but was measured as the distance away from the fiber tip. The weight of the mass along with the known density of stainless-steel was used to calculate the radius of the mass, which was then used to calculate the moment of inertia of the mass

$$M = \gamma_{\text{mass}} * \frac{4}{3}\pi r_{\text{mass}}^3 \tag{17}$$

$$J_{\text{mass}} = \frac{2}{5} M r_{\text{mass}}^2 \tag{18}$$

The mass, moment of inertia, location, and associated uncertainties were used as additional inputs for the mathematical model to obtain predicted resonant frequency ranges of the system with the mass. The output from the mathematical model was again used to provide starting ranges for each resonant frequency for the experimental procedure. The system characteristics are listed in Table 1.

We then used the mathematical model to simulate the resonance frequencies in the horizontal axis for an arbitrary length of fiber with a spherical stainless-steel mass being placed at various locations along the mass, starting at the base of the fiber and moving to the tip in increments of 1% of the fiber length. This simulation was repeated for increasingly heavier masses ($M = 0$ to $M = 15 * m_{\text{fiber}}$) with the corresponding increases in moment of inertia as determined using Eqs. (17) and (18). Figure 3 shows this plot using a 10 mm length of fiber as an example.

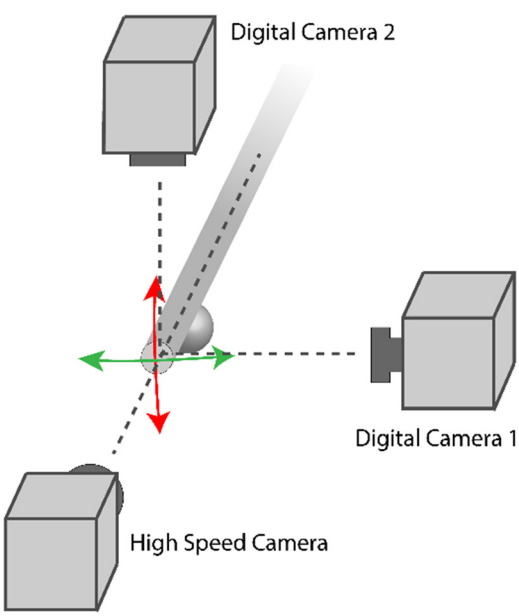

Fig. 2 Diagram of the setup of cameras used to observe the fiber and collect data for the experimental setup. The digital cameras observe the side views of the fiber while being excited to verify the shape of fiber at each resonant frequency. The high-speed camera looked at the tip of the fiber and provided deflection data at each resonant frequency.

Two additional setups each with a different fiber length and added mass were constructed to test two separate conditions simulated in Fig. 3. The first additional system exhibited similar frequency characteristics as seen in the thin dotted lines of Fig. 3 where the frequency peaks align with the nodal points. A fiber near 60 mm and a mass which was less than 4 times the mass of the fiber was used. The second additional system exhibited similar frequency characteristics as seen in the medium thickness dotted line of Fig. 3. With increasing mass and moment of inertia, the frequency peaks of the higher resonant frequencies occur when the mass is located near the antinodes. For this system, a fiber length near 30 mm and a mass which was at least 12 times the weight of the fiber were selected. The exact fiber lengths were determined experimentally by finding the first 10 resonant frequencies then determining the length of fiber for which the mathematical model provides predicted frequencies within the range of observation uncertainty. The characteristics for both additional systems are listed in Table 2.

In both of these setups, initial resonance frequencies without the mass were found, then the mass was attached toward the end of the fiber, the first four resonant frequencies were experimentally determined for the horizontally driven case, then the mass was removed and reattached at a new location, which was further away from the tip of the fiber. Images of the setup with the mass in each location were used to determine the location of the mass as a fraction of the length of the fiber (η). In ImageJ, a line was drawn from the base of the fiber to the tip and the scale was set to 1, then a line from the base to the center of the mass was drawn and measured. This process was repeated with both setups to acquire data points at multiple locations along the fiber.

3 Results

Table 3 compares the mathematical and experimental results of the resonant frequencies for the initial massless fiber system. The predicted values from the mathematical model had a 4.7% error compared to the horizontal axis and a 5.2% error compared to the vertical axis. We calibrated the mathematical model by adjusting the fiber length in each direction to match the experimental observations. Calibrated lengths of 34.745 mm in the horizontal direction and 34.84 mm in the vertical direction were found to agree with the experimental values within the uncertainty range of the observed resonant frequencies. The slight difference in resonant frequencies between the two axes is likely due to the asymmetry of the fiber glued into the piezo.

The resonant frequencies for the initial system with the mass were calculated both without and with the length calibration. For the uncalibrated model, the original fiber length measurement and the mass weight with associated uncertainties were used and the mass placement was assumed to be at the nominal third resonant node location ($0.868 * l$). These calculated values are listed in Table 4 as Math-H for the horizontally driven direction, and Math-V for the vertically driven direction. For the calibrated model, the calibrated lengths found from the massless system in

Table 1 Initial test system characteristics for a mass located near the third harmonic nodal point

Property	Values
Fiber length	34.0 ± 0.5 mm
Added mass	4.50 ± 0.05 mg
Mass radius	0.51 ± 0.004 mm
Mass location	4.55 ± 0.03 mm From fiber tip

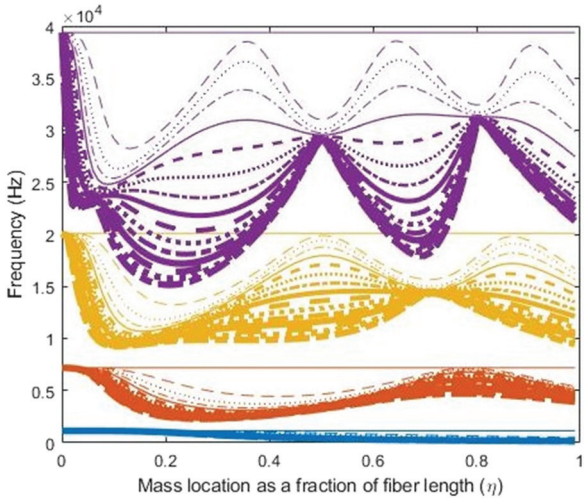

Fig. 3 Simulation of a 10 mm fiber with an attached spherical stainless-steel mass, which increases in both mass and moment of inertia as the mass location is moved along the length of the fiber. The colors indicate different resonant modes (blue—first, orange—second, yellow—third, purple—fourth). The increase in mass and associated moment of inertia are indicated by gradually thicker lines from a minimum of $M = J = 0$ to a maximum of $M = 15 * M_{\text{fiber}}$ with the radius determined by rearranging Eq. (17) and moment of inertia found using Eq. (18).

Table 2 Characteristics for the two additional systems

Property	System 1	System 2
Fiber length	30.99 mm	58.35 mm
Added mass	13.00 ± 0.05 mg	4.50 ± 0.05 mg

Table 3 Resonant frequencies predicted by mathematical calculation (Math) and the experimental data for the described system without an attached mass (exp.-H and exp.-V)

	Math	Math Adj.-H	Exp.-H	Math Adj.-V	Exp.-V
First	84.8–90.0	83.6	83.6 ± 0.1	83.2	83.1 ± 0.1
Second	531.7–563.9	524.4	524.6 ± 0.5	521.8	521.7 ± 0.5
Third	1488.8–1579.0	1468.4	1468.4 ± 1.5	1461.2	1461.2 ± 1.5
Fourth	2917.5–3094.2	2877.6	2877.8 ± 2.9	2863.4	2862.9 ± 2.9

Once experimental values were acquired, values for the length in each driving direction were adjusted to match within the range of observation uncertainty (math adj.-H and math adj.-V).

addition to the mass and its physically measured location along with the error measurements were used as inputs into the mathematical model to find an appropriate range of frequencies. The calibrated mathematical models of the system with the mass are listed as math adjusted-H and math adjusted-V for the horizontal and vertical directions in Table 4. The experimental measurements are listed as exp.-H and Exp.-V for the horizontal and vertical directions, respectively. This shows a maximum error of 6.6% for the uncalibrated calculated frequencies to the experimentally found frequencies, and a maximum error of 1.5% from the calibrated frequencies to the experimentally found frequencies. The residual error in the calibrated model is likely due to the difference between the assumed mass location and the real mass location.

Images of the fiber shape were taken at all resonant modes both with and without the attached mass. By comparing the observed fiber shape to the expected shape for each resonant frequency mode, we were able to ensure that the correct resonant frequency had been found. Figure 4 shows images of the fiber shapes at each resonant frequency for both the massless system and the system with an attached mass.

The measurements of the amplitude showed an approximately linear increase in deflection as a function of voltage for every resonant frequency. Deflection of the fiber when excited at the first resonant frequency increased as a result of adding the mass but decreased for all other resonant frequencies as shown in Fig. 5.

For the additional two systems, the fiber was cleaved to an approximate length, then the resonance frequencies were found experimentally. We found the calibrated length using the experimental data. The calibrated length and mass for both cases were used as inputs to the mathematical model to produce graphs of resonance frequencies as a function of mass location. The theoretical graphs and experimental data for each system have been plotted together in Fig. 6.

4 Discussion

These experiments showed that the described mathematical calculations can predict resonant frequencies of a piezofiber system with an intermediate mass within 10% of the experimental values up to the fourth resonant frequency without building and testing the system first. If measurements on the constructed massless system are acquired, predictions may be even better. It is possible that the predictions above the fourth resonant frequency are also in good agreement with the physical system. However, due to the small deflection of the fiber tip, the higher resonant frequencies were experimentally unidentifiable.

For the initial experimental setup the tip deflection of the fiber when excited at the first resonant frequency with the added mass was more than double the tip deflection of the massless system. This amplitude increase is likely a combined effect of the increased momentum due to the mass as well as the lowered frequency. For the higher-order modes, the mass acted as a forced nodal point at a location that may not have coincided with the

Table 4 Comparison of mathematical calculation and experimental data for the system with an attached mass located 4.493 mm from the fiber tip

	Math-H	Math Adj.-H	Exp.-H	Math-V	Math Adj.-V	Exp.-V
First	22.4–23.62	22.0–22.3	22.4 ± 0.2	22.3–23.6	21.9–22.2	22.3 ± 0.2
Second	481.4–510.2	473.3–474.9	470.4 ± 0.5	463.7–490.5	453.8–455.8	449.7 ± 0.4
Third	1429.2–1512.6	1410.4–1412.6	1400.4 ± 1.4	1265.5–1331.8	1246.1–1252.2	1257.0 ± 1.3
Fourth	2547.1–2694.1	2515.2–2530.6	2564.4 ± 2.6	2287.8–2415.1	2247.5–2256.6	2236.2 ± 2.2

Math-H and math-V are the predicted frequencies from the mathematical model using the base assumptions of no damping, using the measured fiber length, the mass of the bead, and assuming ideal location at $0.868l$ in the horizontal and vertical directions, respectively. Math adj.-H and math adj.-V are the predicted frequencies from the mathematical model using the calibrated fiber length in addition to the mass and the measured mass location for the horizontal and vertical directions, respectively. Exp.-H and exp-V. are the experimentally found resonant frequencies for the horizontal and vertical directions, respectively.

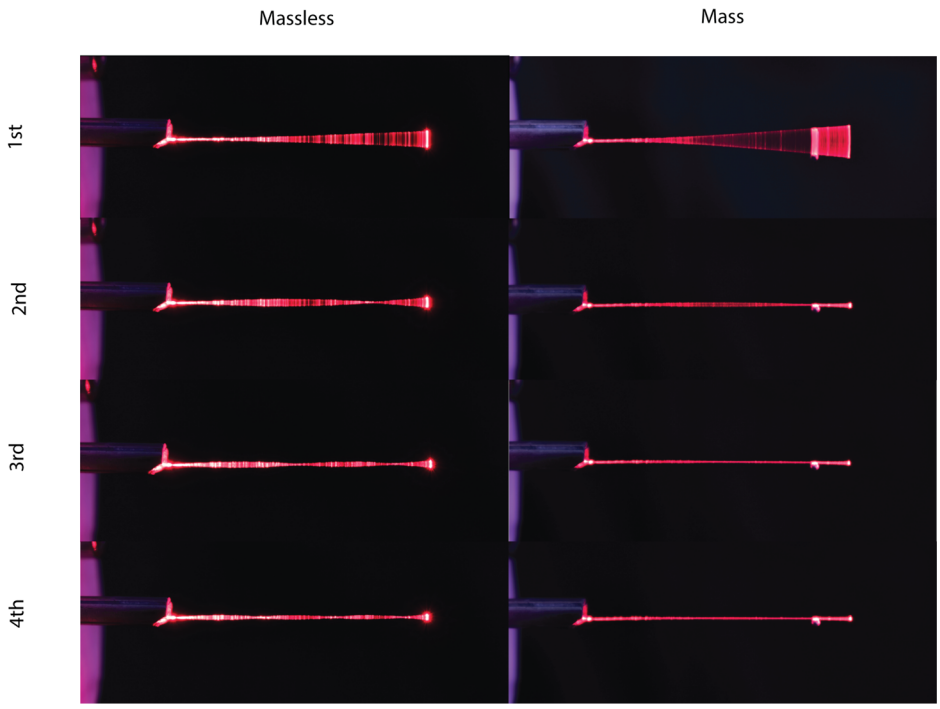

Fig. 4 Long exposure images of the fiber vibrating at the first through the fourth resonant modes. A 642 nm laser diode is coupled into the fiber for ease of visualization. The images on the left are the massless fiber system, and the images on the right are the fiber with the mass.

exact natural nodal point causing less deflection. However, in the horizontal direction, where the mass is near the natural nodal point and the CoM was aligned with the fiber, the average percent decrease in deflection between the system without and with the mass is less for the third resonant frequency (26.8%) than it is for the second (62.8%) or fourth (31.4%) resonant frequencies.

If a point mass is assumed, then the resonant frequency would reach its original massless value whenever the mass is located at a corresponding nodal point [20,21]. For a mass with a small moment of inertia, the general trend holds true where the resonant frequency becomes closer to the original value when placed at a nodal point [22]. This trend was verified as shown in the plot on

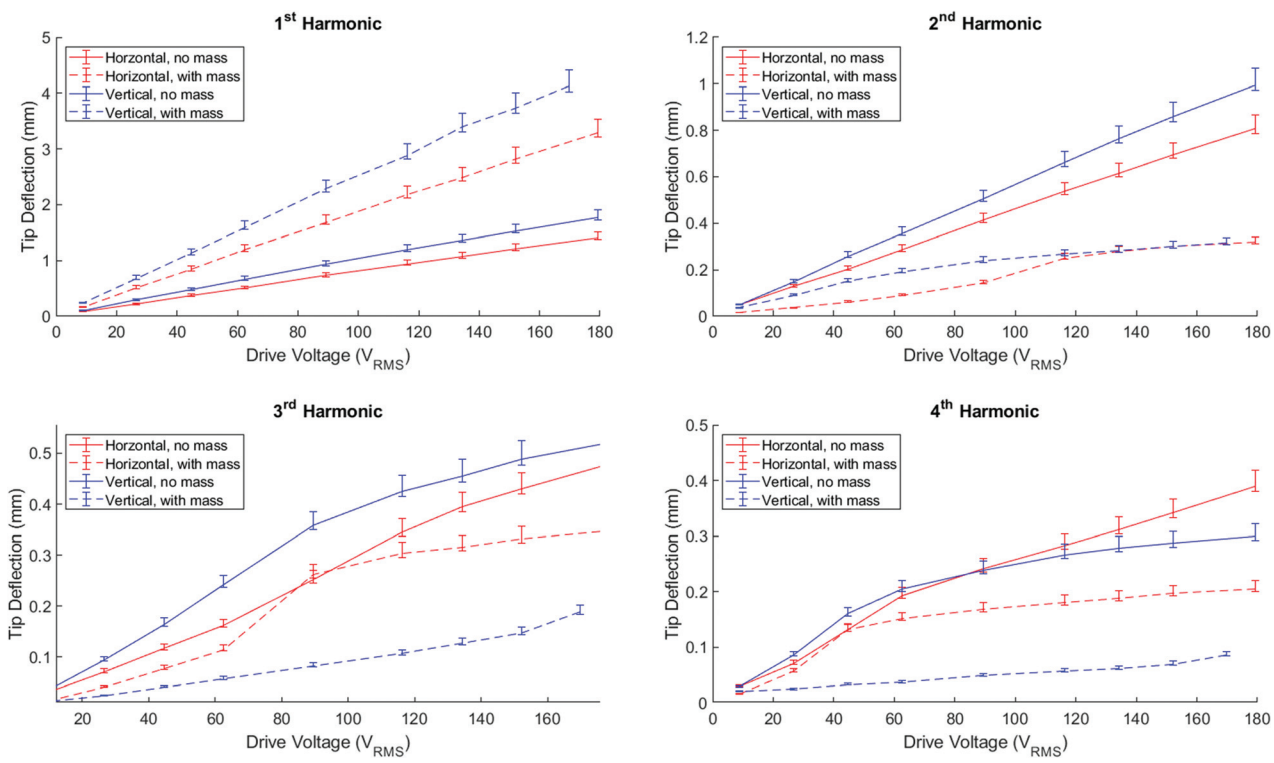

Fig. 5 Plots of the tip deflection as the applied voltage is increased. Each plot is for one of the resonant modes showing the system driven in both the horizontal and vertical directions, for both the massless fiber system and the system with the mass.

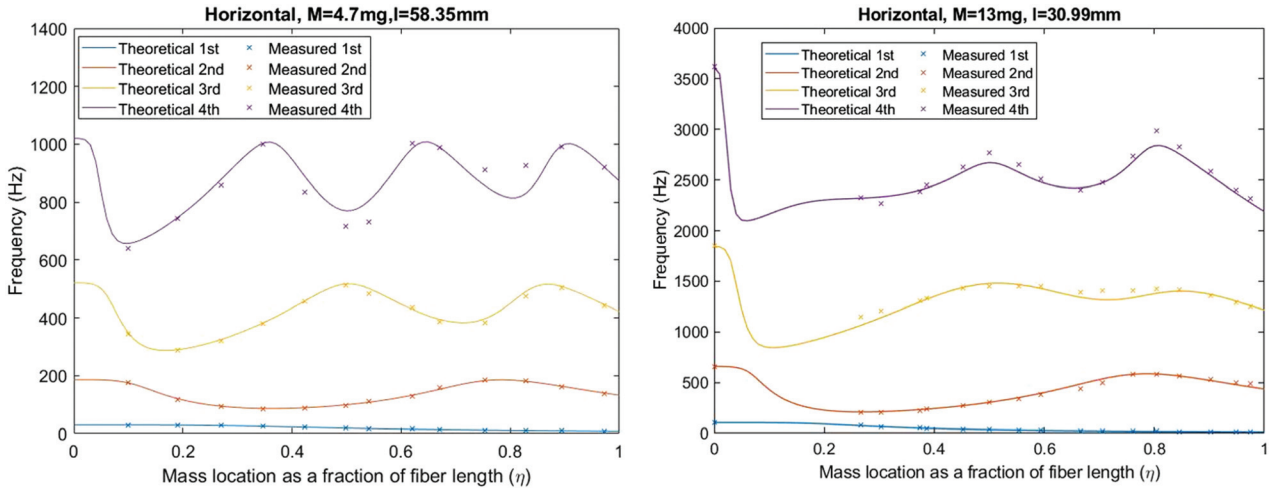

Fig. 6 Theoretical and measured data of resonant frequencies as a function of mass location along the fiber. The plot on the left is for a longer fiber (59.35 mm) and a smaller mass (4.7 mg). The plot on the right is a shorter fiber (30.99 mm) and larger mass (13 mg).

the left of Fig. 6. If a theoretical massless element with a moment of inertia were attached to a beam, the highest resonant frequencies happen when the element is located near the antinode [21].

A physical element with both mass and moment of inertia will have resonant frequency characteristics between these two theoretical cases as shown in Fig. 3. A mass with a large enough moment of inertia can cause the inversion of the peaks where the peaks of the frequency curve are no longer when the mass is placed at the nodal points, but rather when the mass is placed at the antinodes. This trend was verified as shown in the plot on the right of Fig. 6 where the fourth resonance frequency curve inverted with a mass that was 15.8 times the mass of the fiber. The moment of inertia of the mass inhibits rotation. When positioned at a nodal point, where there is the highest amount of rotation, it is likely that the beam is unable to provide the required bending moment at that location. As a result, the nodal point may shift, and the resonant frequency will decrease. The size and weight of a mass needed to cause the inversion of the frequency curves is dependent on the beam properties and dimensions.

Whirling was observed near resonant frequencies for all constructed systems. The whirling in the massless systems was more stable and occurred over a broader frequency range than the systems with the mass. The systems with the mass exhibited unstable whirling motion but only over a narrow range of frequencies. This is expected due to the asymmetry of the mass which changes the resonant frequencies of the two directions and dampens the off-axis motion [23].

5 Conclusion

The mathematical model presented here can be a powerful design tool for scanning systems, which utilize cantilevered fibers driven at multiple resonant frequencies. The results suggest that piezo-driven scanning fiber systems may be driven at the first and a higher order frequency where the ratio between the frequencies of the modes may be chosen by design. A fast axis moving on the order of a few kHz and a slow axis moving on the order of 10 s of Hz enables the use of raster scanning patterns for endoscopic imaging systems. The increased deflection of the first resonant frequency with an added mass helps reduce the voltage requirement for the slow scanning axis. The moment of inertia and location of an added mass can significantly alter the frequency response of the system. This is more drastic at the higher order modes. A mass with a small moment of inertia placed at a natural nodal point will have only a minor impact on the corresponding resonant frequency. However, if a large mass is to be used in order to lower the first resonant frequency, an inversion in the higher order resonance frequency curves may occur. With an asymmetric mass, the suppression of the whirling motion at higher order modes when driven slightly off resonance is advantageous for image reconstruction if the proper amplitude is achieved. The mathematical model outlined in this paper can be used to optimize a scanning system with an arbitrary intermediate mass with final resonance frequencies being within 10% of the predicted values.

Acknowledgment

The authors appreciate helpful discussions with Mr. Ali Kamali and Dr. Kaveh Laksari. Any opinions, findings, and conclusions or recommendations expressed in this material are those of the author(s) and do not necessarily reflect the views of the National Institutes of Health or National Science Foundation.

Funding Data

- National Institute of Biomedical Imaging and Bioengineering of the National Institutes of Health (Award No. 1R01EB020605; Funder ID: 10.13039/100000002).
- National Science Foundation Graduate Research Fellowship Program (Grant No. DGE-1746060 and DGE-1143953; Funder ID: 10.13039/100000001).

Conflict of Interest

There are no conflict of interest.

Appendix: Generalized Cantilevered Beam Equations

Hamdan et al. provided information for a system with one intermediate mass and an end mass [17]. In the main text, we used the boundary conditions from this literature to arrive at the system of linear equations provided in matrix form by setting all boundary conditions referring to an end mass to zero, as our setup did not have an end mass. Here, we reiterate the boundary conditions provided by Hamdan et al. and provide the resulting system of linear equations for a setup with one intermediate mass and an end mass. We then expand upon the approach of dividing the beam into segments to provide a generalized system of linear equations for any number of intermediate masses with the option of an end mass.

End Mass

Here, we consider a cantilevered beam with an intermediate mass and an end mass as shown in Fig. 7.

The following boundary conditions at $x_2 = l(1-\eta)$ replace Eqs. (13) and (14) in the main text:

$$EI\frac{dy_2^2(x_2 = l(1-\eta))}{dx_2^2} = J_e\omega^2\frac{dy_2(x_2 = l(1-\eta))}{dx_2} \tag{A1}$$

$$EI\frac{dy_2^3(x_2 = l(1-\eta))}{dx_2^3} = -\omega^2 M_e y_2(x_2 = l(1-\eta)) \tag{A2}$$

Here, Je and M_e are the moment of inertia and the mass of the end mass, respectively. The resulting system of equation matrix is as follows:

$$\begin{bmatrix} 0 & 1 & 0 & 1 & 0 & 0 & 0 & 0 \\ 1 & 0 & 1 & 0 & 0 & 0 & 0 & 0 \\ \sin(Z_1) & \cos(Z_1) & \sinh(Z_1) & \cosh(Z_1) & 0 & -1 & 0 & -1 \\ \cos(Z_1) & -\sin(Z_1) & \cosh(Z_1) & \sinh(Z_1) & -1 & 0 & -1 & 0 \\ -A\gamma\sin(Z_1) & -A\gamma\cos(Z_1) & A\gamma\sinh(Z_1) & A\gamma\cosh(Z_1) & 0 & A\gamma & 0 & -A\gamma \\ -J\Lambda^3\cos(Z_1) & +J\Lambda^3\sin(Z_1) & -J\Lambda^3\cosh(Z_1) & -J\Lambda^3\sinh(Z_1) & A\gamma & 0 & -A\gamma & 0 \\ -A\gamma\cos(Z_1) & A\gamma\sin(Z_1) & A\gamma\cosh(Z_1) & A\gamma\sinh(Z_1) & -A\gamma\sin(Z_2) & -A\gamma\cos(Z_2) & A\gamma\sinh(Z_2) & A\gamma\cosh(Z_2) \\ +M\Lambda\sin(Z_1) & +M\Lambda\cos(Z_1) & +M\Lambda\sinh(Z_1) & +M\Lambda\cosh(Z_1) & -J_e\Lambda^3\cos(Z_2) & +J_e\Lambda^3\sin(Z_2) & -J_e\Lambda^3\cosh(Z_2) & -J_e\Lambda^3\sinh(Z_2) \\ 0 & 0 & 0 & 0 & -A\gamma\cos(Z_2) & A\gamma\sin(Z_2) & A\gamma\cosh(Z_2) & A\gamma\sinh(Z_2) \\ 0 & 0 & 0 & 0 & +M_e\Lambda\sin(Z_2) & +M_e\Lambda\cos(Z_2) & +M_e\Lambda\sinh(Z_2) & +M_e\Lambda\cosh(Z_2) \end{bmatrix}$$

The determinant of this matrix is then set to zero and solutions for Λ can be found, the same way as is described in the main text.

Multiple Intermediate Masses

This set of equations can be generalized further for a system with N number of integer masses and an end mass. This system can be visualized in Fig. 8.

Each segment of the beam follows the differential equation for simple resonant motion:

$$\frac{d^4 y_i}{dx_i^4} - \Lambda^4 y_i(x_i) = 0, \text{ for } 0 \le x_i \le l\eta_i \tag{A3}$$

$$\frac{d^4 y_{N+1}}{dx_{N+1}^4} - \Lambda^4 y_{N+1}(x_{N+1}) = 0 \text{ for } 0 \le x_{N+1} \le l\left(1 - \sum_{i=1}^{N}\eta_i\right) \tag{A4}$$

Equation (A3) describes the segment of beam between intermediate mass $i-1$ and intermediate mass i from $i=1$ up to N. Equation (A4) describes the final segment of the beam from the final intermediate mass to the end mass or the end of the beam if no end mass is present. As before the solution to this differential equation for each segment is

Fig. 7 Cantilevered beam system with one intermediate mass and an end mass

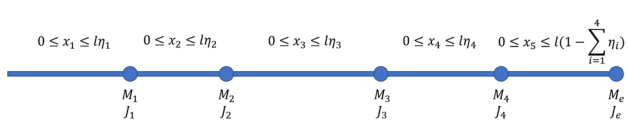

Fig. 8 System with $N=4$ intermediate masses and an end mass

$$\begin{aligned} y_i(x_i) =& A_{(j+1)}\sin(\Lambda x_i) + A_{(j+2)}\cos(\Lambda x_i) \\ &+ A_{(j+3)}\sin h(\Lambda x_i) + A_{(j+4)}\cos h(\Lambda x_i) \end{aligned} \tag{A5}$$

$$j = 4(i-1) \text{ for } 1 \le i \le N+1 \tag{A6}$$

The boundary conditions are applied at each intermediate mass as follows:

$$y_1(x_1 = 0)) = 0 \tag{A7}$$

$$\frac{dy_1(x_1 = 0)}{dx_1} = 0 \tag{A8}$$

$$y_i(x_i = l\eta_i) = y_{i+1}(x_{i+1} = 0) \tag{A9}$$

$$\frac{dy_i(x_i = l\eta_i)}{dx_i} = \frac{dy_{i+1}(x_{i+1} = 0)}{dx_{i+1}} \tag{A10}$$

$$\begin{aligned} EI\frac{dy_i^2(x_i = l\eta_i)}{dx_i^2} - EI\frac{dy_{i+1}^2(x_{i+1} = 0)}{dx_{i+1}^2} \\ = J_i\omega^2\frac{dy_i(x_i = l\eta_i)}{dx_i} \end{aligned} \tag{A11}$$

$$\begin{aligned} EI\frac{dy_i^3(x_i = l\eta_i)}{dx_i^3} - EI\frac{dy_{i+1}^3(x_{i+1} = 0)}{dx_{i+1}^3} \\ = -\omega^2 M_i y_i(x_i = l\eta_i) \end{aligned} \tag{A12}$$

$$\begin{aligned} EI\frac{dy_{N+1}^2\left(x_{N+1} = l\left(1 - \sum_{i=1}^{N}\eta_i\right)\right)}{dx_{N+1}^2} \\ = J_e\omega^2\frac{dy_{N+1}\left(x_{N+1} = l\left(1 - \sum_{i=1}^{N}\eta_i\right)\right)}{dx_{N+1}} \end{aligned} \tag{A13}$$

$$EI\frac{dy_{N+1}^3\left(x_{N+1}=l\left(1-\sum_{i=1}^{N}\eta_i\right)\right)}{dx_{N+1}^3}=-\omega^2 M_e y_{N+1}\left(x_{N+1}=l\left(1-\sum_{i=1}^{N}\eta\right)\right) \tag{A14}$$

This results in a system of equations that can be put into an MxM matrix, where $M = 4 * (N + 1)$. There are four unique submatrices which comprise the full system of equations matrix

$$\textbf{Start}=\begin{bmatrix}0 & 1 & 0 & 1\\ 1 & 0 & 1 & 0\end{bmatrix}\quad \boldsymbol{B_i}=\begin{bmatrix}\sin Z_i & \cos Z_i & \sinh Z_i & \cosh Z_i\\ \cos Z_i & -\sin Z_i & \cosh Z_i & \sinh Z_i\\ \begin{matrix}-A\gamma\sin(Z_i)\\ -J_i\Lambda^3\cos(Z_i)\end{matrix} & \begin{matrix}-A\gamma\cos(Z_i)\\ +J_i\Lambda^3\sin(Z_i)\end{matrix} & \begin{matrix}A\gamma\sinh(Z_i)\\ -J_i\Lambda^3\cosh(Z_i)\end{matrix} & \begin{matrix}A\gamma\cosh(Z_i)\\ -J_i\Lambda^3\sinh(Z_i)\end{matrix}\\ \begin{matrix}-A\gamma\cos(Z_i)\\ +M_i\Lambda\sin(Z_i)\end{matrix} & \begin{matrix}A\gamma\sin(Z_i)\\ +M_i\Lambda\cos(Z_i)\end{matrix} & \begin{matrix}A\gamma\cosh(Z_i)\\ +M_i\Lambda\sinh(Z_i)\end{matrix} & \begin{matrix}A\gamma\sinh(Z_i)\\ +M_i\Lambda\cosh(Z_i)\end{matrix}\end{bmatrix}$$

Here, $Z_i = l\eta_i$, J_i and M_i are the moment of inertia and mass of mass i, respectively. A and γ are the cross-sectional area and the density of the beam material

$$\boldsymbol{C}=\begin{bmatrix}0 & -1 & 0 & -1\\ -1 & 0 & -1 & 0\\ 0 & A\gamma & 0 & -A\gamma\\ A\gamma & 0 & -A\gamma & 0\end{bmatrix}\quad \textbf{End}=\begin{bmatrix}\begin{matrix}-A\gamma\sin(Z_e)\\ -J_e\Lambda^3\cos(Z_e)\end{matrix} & \begin{matrix}-A\gamma\cos(Z_e)\\ +J_e\Lambda^3\sin(Z_e)\end{matrix} & \begin{matrix}A\gamma\sinh(Z_e)\\ -J_e\Lambda^3\cosh(Z_e)\end{matrix} & \begin{matrix}A\gamma\cosh(Z_e)\\ -J_e\Lambda^3\sinh(Z_e)\end{matrix}\\ \begin{matrix}-A\gamma\cos(Z_e)\\ +M_e\Lambda\sin(Z_e)\end{matrix} & \begin{matrix}A\gamma\sin(Z_e)\\ +M_e\Lambda\cos(Z_e)\end{matrix} & \begin{matrix}A\gamma\cosh(Z_e)\\ +M_e\Lambda\sinh(Z_e)\end{matrix} & \begin{matrix}A\gamma\sinh(Z_e)\\ +M_e\Lambda\cosh(Z_e)\end{matrix}\end{bmatrix}$$

where $Z_e = l(1 - \sum_{i=1}^{N}\eta_i)$. Repeating $\boldsymbol{B_i}$ and $\boldsymbol{C}$ for as many intermediate masses are present in the system combined with the **Start** and **End** matrices in the following way to form the full system of linear equations:

$$\begin{bmatrix}\textbf{Start} & \dots & \dots & \dots & 0\\ \boldsymbol{B_1} & \boldsymbol{C} & & & \vdots\\ \vdots & \boldsymbol{B_2} & \boldsymbol{C} & & \vdots\\ \vdots & & \ddots & \ddots & \vdots\\ \vdots & & & \boldsymbol{B_N} & \boldsymbol{C}\\ 0 & \dots & \dots & \dots & \textbf{End}\end{bmatrix}$$

The same process as described in the main text may be used to find the resonant frequencies of the system by setting the determinant of this matrix to zero and solving for Λ.

References

[1] Li, Z., and Fu, L., 2012, "Note: A Resonant Fiber-Optic Piezoelectric Scanner Achieves a Raster Pattern by Combining Two Distinct Resonances," Rev. Sci. Instrum., **83**(8), p. 086102.

[2] Lee, C. M., Engelbrecht, C. J., Soper, T. D., Helmchen, F., and Seibel, E. J., 2010, "Scanning Fiber Endoscopy With Highly Flexible, 1 mm Catheterscopes for Wide-Field, Full-Color Imaging," J. Biophotonics, **3**(5–6), pp. 385–407.

[3] Liang, W., Murari, K., Zhang, Y. Y., Chen, Y., Li, X. D., and Li, M.-J., 2012, "Increased Illumination Uniformity and Reduced Photodamage Offered by the Lissajous Scanning in Fiber-Optic Two-Photon Endomicroscopy," J. Biomed. Opt., **17**(2), p. 021108.

[4] Zhang, N., Tsai, T.-H., Ahsen, O. O., Liang, K., Lee, H.-C., Xue, P., Li, X., and Fujimoto, J. G., 2014, "Compact Piezoelectric Transducer Fiber Scanning Probe for Optical Coherence Tomography," Opt. Lett., **39**(2), pp. 186–188.

[5] Lurie, K. L., Gurjarpadhye, A. A., Seibel, E. J., and Ellerbee, A. K., 2015, "Rapid Scanning Catheterscope for Expanded Forward-View Volumetric Imaging With Optical Coherence Tomography," Opt. Lett., **40**(13), pp. 3165–3168.

[6] Akhoundi, F., Qin, Y., Peyghambarian, N., Barton, J. K., and Kieu, K., 2018, "Compact Fiber-Based Multi-Photon Endoscope Working at 1700 nm," Biomed. Opt. Express, **9**(5), pp. 2326–2335.

[7] Vega, D., Kiekens, K. C., Syson, N. C., Romano, G., Baker, T., and Barton, J. K., 2018, "Full Optical Model of Micro-Endoscope With Optical Coherence Microscopy, Multiphoton Microscopy and Visible Capabilities," *Endoscopic Microscopy XIII*, J. Guillermo, M. D. Tearney, T. D. Wang, and M. J. Suter, eds., Vol. 10470, International Society for Optics and Photonics, SPIE, Bellingham, WA, pp. 7–20.

[8] Tate, T. H., Baggett, B., Rice, P. F. S., Koevary, J. W., Orsinger, G. V., Nymeyer, A. C., Welge, W. A., Saboda, K., Roe, D. J., Hatch, K. D., Chambers, S. K., Utzinger, U., and Barton, J. K., 2016, "Multispectral Fluorescence Imaging of Human Ovarian and Fallopian Tube Tissue for Early-Stage Cancer Detection," J. Biomed. Opt., **21**(5), pp. 056005–9.

[9] Hariri, L. P., Bonnema, G. T., Schmidt, K., Winkler, A. M., Korde, V., Hatch, K. D., Davis, J. R., Brewer, M. A., and Barton, J. K., 2009, "Laparoscopic Optical Coherence Tomography Imaging of Human Ovarian Cancer," Gynecol. Oncol., **114**(2), pp. 188 –194.

[10] Watson, J. M., Marion, S. L., Rice, P. F., Utzinger, U., Brewer, M. A., Hoyer, P. B., and Barton, J. K., 2013, "Two-Photon Excited Fluorescence Imaging of Endogenous Contrast in a Mouse Model of Ovarian Cancer," Lasers Surg. Med., **45**(3), pp. 155–166.

[11] Sawyer, T. W., Luthman, A. S., and Bohndiek, S. E., 2017, "Evaluation of Illumination System Uniformity for Wide-Field Biomedical Hyperspectral Imaging," J. Opt., **19**(4), p. 045301.

[12] Sawyer, T. W., Koevary, J. W., Rice, F. P. S., Howard, C. C., Austin, O. J., Connolly, D. C., Cai, K. Q., and Barton, J. K., 2019, "Quantification of Multiphoton and Fluorescence Images of Reproductive Tissues From a Mouse Ovarian Cancer Model Shows Promise for Early Disease Detection," J. Biomed. Opt., **24**(09), pp. 1–16.

[13] Seibel, E. J., Fauver, M., Crossman-Bosworth, J. L., Smithwick, Q. Y. J., and Brown, C. M., 2003, "Microfabricated Optical Fiber With a Microlens That Produces Large Field-of-View Video-Rate Optical Beam Scanning for Microendoscopy Applications," *Optical Fibers and Sensors for Medical Applications III*, I. Gannot, ed., Vol. 4957, International Society for Optics and Photonics, SPIE, Bellingham, WA, pp. 46–55.

[14] Huo, L., Xi, J., Wu, Y., and Li, X., 2010, "Forward-Viewing Resonant Fiber-Optic Scanning Endoscope of Appropriate Scanning Speed for 3D OCT Imaging," Opt. Express, **18**(14), pp. 14375–14384.

[15] Moon, S., Lee, S.-W., Rubinstein, M., Wong, B. J. F., and Chen, Z., 2010, "Semi-Resonant Operation of a Fiber-Cantilever Piezotube Scanner for Stable Optical Coherence Tomography Endoscope Imaging," Opt. Express, **18**(20), pp. 21183–21197.

[16] Mei, C., 2012, "Studying the Effects of Lumped End Mass on Vibrations of a Timoshenko Beam Using a Wave-Based Approach," J. Vib. Control, **18**(5), pp. 733–742.

[17] Hamdan, M., and Latif, L., 1994, "On the Numerical Convergence of Discretization Methods for the Free Vibrations of Beams With Attached Inertia Elements," J. Sound Vib., **169**(4), pp. 527–545.
[18] Hongjin, W., Qingfeng, M., and Wuwei, F., 2014, "Discussion of the Improved Methods for Analyzing a Cantilever Beam Carrying a Tip-Mass Under Base Excitation," Shock Vib., **2014**, pp. 1–15.
[19] Sun, W., Liu, Y., Li, H., and Pan, D., 2013, "Determination of the Response Distributions of Cantilever Beam Under Sinusoidal Base Excitation," J. Phys.: Conf. Ser., **448**, p. 012010.
[20] Park, S., Chung, W., Youm, Y., and Lee, J., 2000, "Natural Frequencies and Ope-Loop Responses of an Elastic Beam Fixed on a Moving Cart and Carrying an Intermediate Lumped Mass," J. Sound Vib., **230**(3), pp. 591 –615.
[21] Posiadała, B., 1997, "Free Vibrations of Uniform Timoshenko Beams With Attachments," J. Sound Vib., **204**(2), pp. 359–369.
[22] Dohn, S., Sandberg, R., Svendsen, W., and Boisen, A., 2005, "Enhanced Functionality of Cantilever Based Mass Sensors Using Higher Modes," Appl. Phys. Lett., **86**(23), p. 233501.
[23] Haight, E. C., and King, W. W., 1971, "Stability of Nonlinear Oscillations of an Elastic Rod," J. Acoust. Soc. Am., **49**(1A), pp. 83–83.